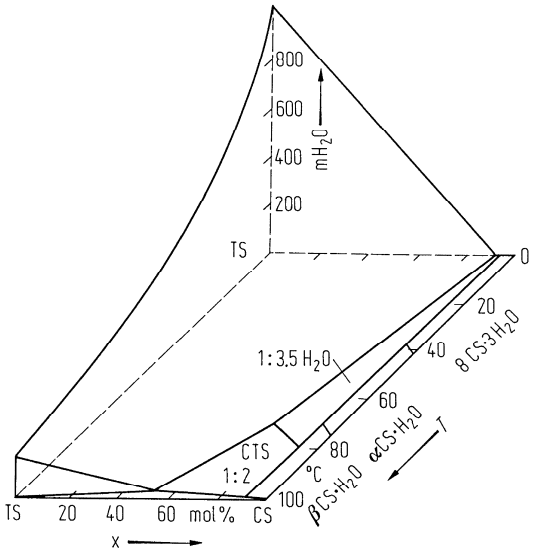

Fig. 43A-15-001. $Tl_2Cd_2(SO_4)_3$. Phase diagram of Tl_2SO_4–$CdSO_4$–H_2O system [74Bre]. TS = Tl_2SO_4, CS = $CdSO_4$, 1:2 = $Tl_2Cd_2(SO_4)_3$, 1:3.5 H_2O = $Tl_2Cd_2(SO_4)_3 \cdot 5H_2O$. It is noticed that $Tl_2Cd_2(SO_4)_3$ crystallizes only above 80 ºC. x: concentration of CS. mH_2O is in equilibrium with $1/b$ moles of the solid phase of composition given in the diagram; b equals the sum of the moles of the starting compounds TC and CS, contained in the solid phase.

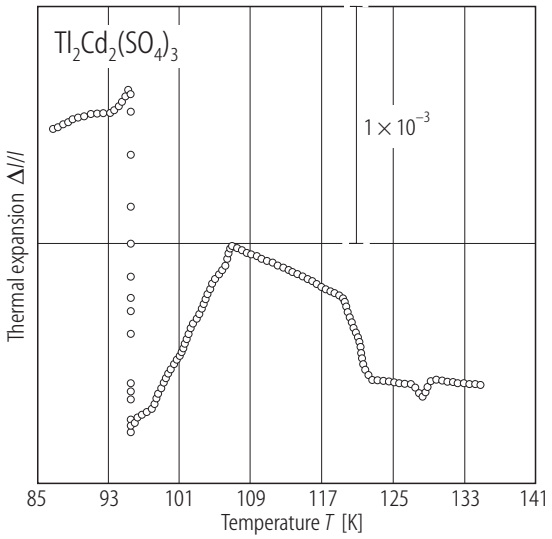

Fig. 43A-15-002. $Tl_2Cd_2(SO_4)_3$. $\Delta l/l$ vs. T [88Kah]. $\Delta l/l$: linear thermal expansion along the ⟨111⟩ axis. Relative to the brass dilatometer cell.

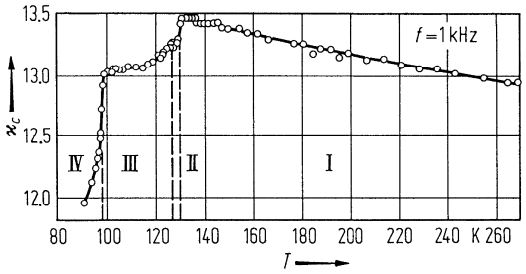

Fig. 43A-15-003. $Tl_2Cd_2(SO_4)_3$. κ_c vs. T [72Bre].

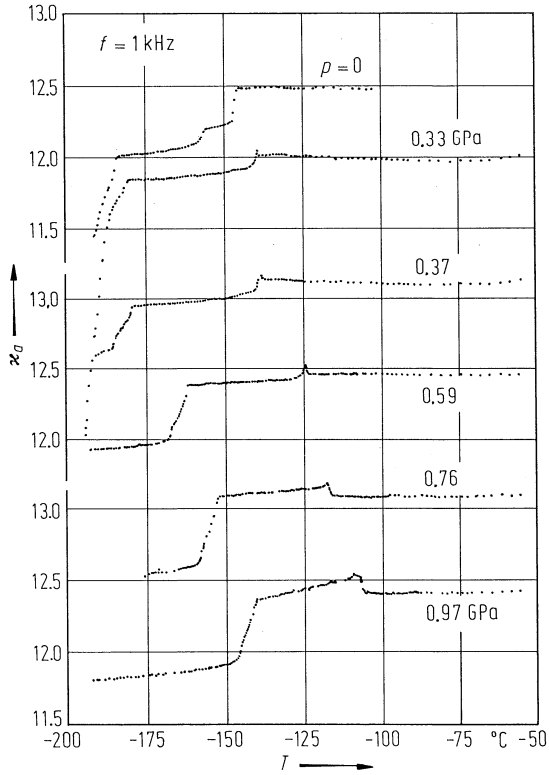

Fig. 43A-15-004. $Tl_2Cd_2(SO_4)_3$. κ_a vs. T [80Hik]. Parameter: p.

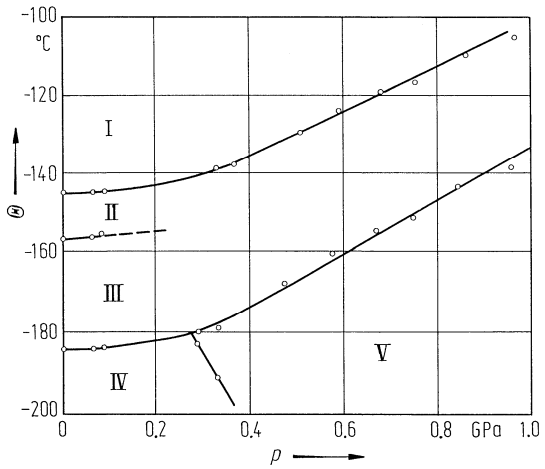

Fig. 43A-15-005. $Tl_2Cd_2(SO_4)_3$. Θ vs. p [80Hik].

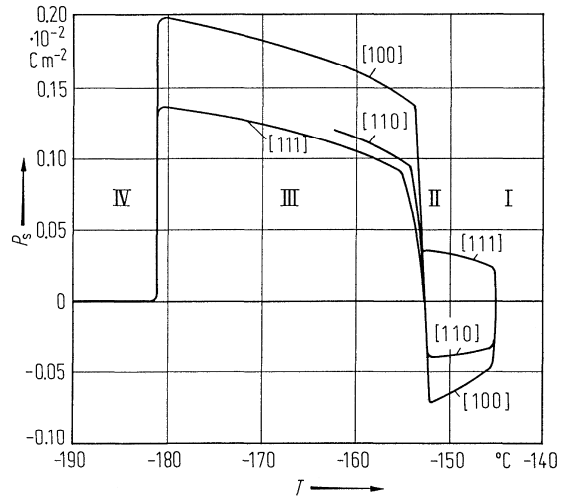

Fig. 43A-15-006. $Tl_2Cd_2(SO_4)_3$. P_s vs. T [80Yam]. Pyroelectric charge method. The zone axes indicated in the figure refer to cubic axes.

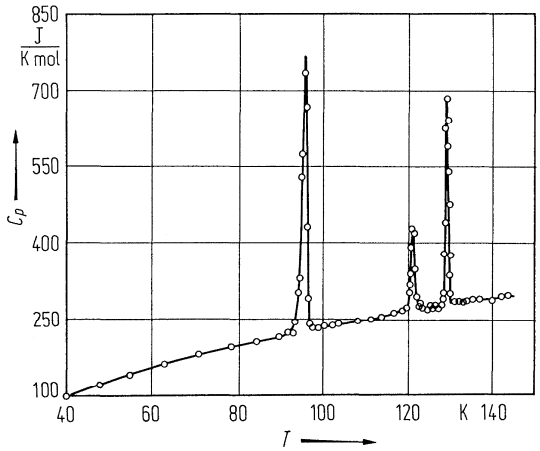

Fig. 43A-15-007. $Tl_2Cd_2(SO_4)_3$. C_p vs. T [75Fra]. C_p: molar specific heat at constant pressure.

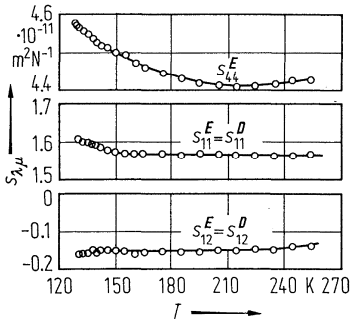

Fig. 43A-15-008. $Tl_2Cd_2(SO_4)_3$. $s_{\lambda\mu}$ vs. T ($T > \Theta_f$) [74Glo].

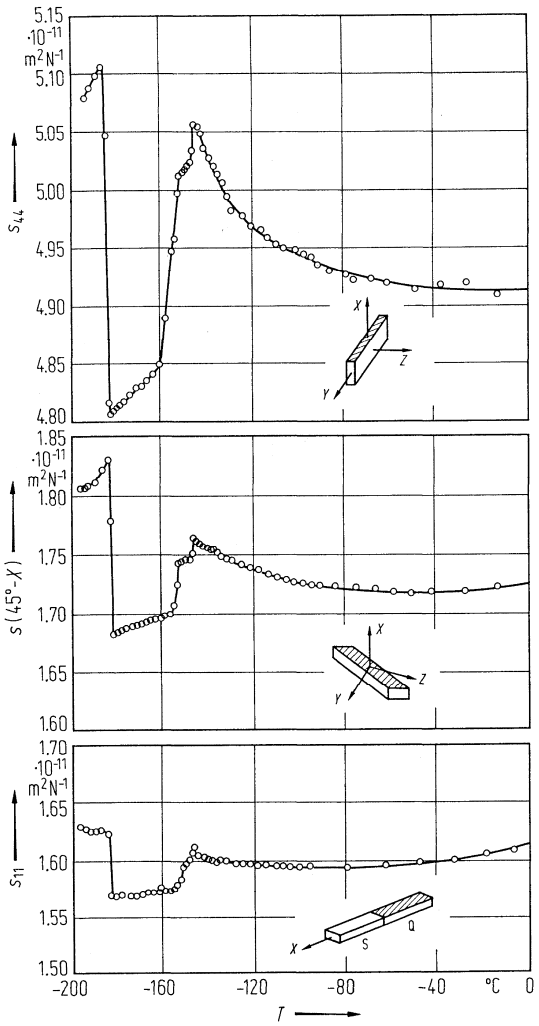

Fig. 43A-15-009. $Tl_2Cd_2(SO_4)_3$. s vs. T [75Ike]. s: elastic compliance, $s(45° - X)$: that for 45° X-cut bar. S: specimen, Q: quartz transducer.

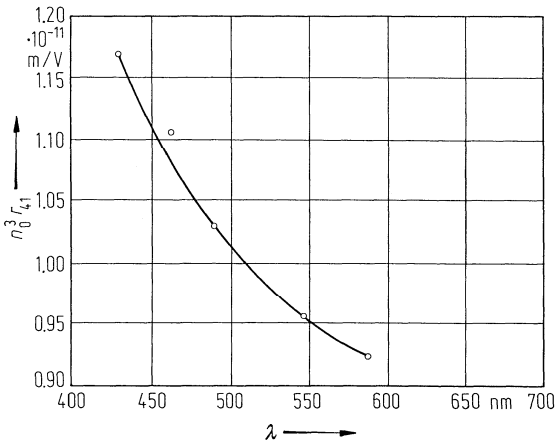

Fig. 43A-15-010. $Tl_2Cd_2(SO_4)_3$. $n_0^3 r_{41}$ vs. λ [69Vas].

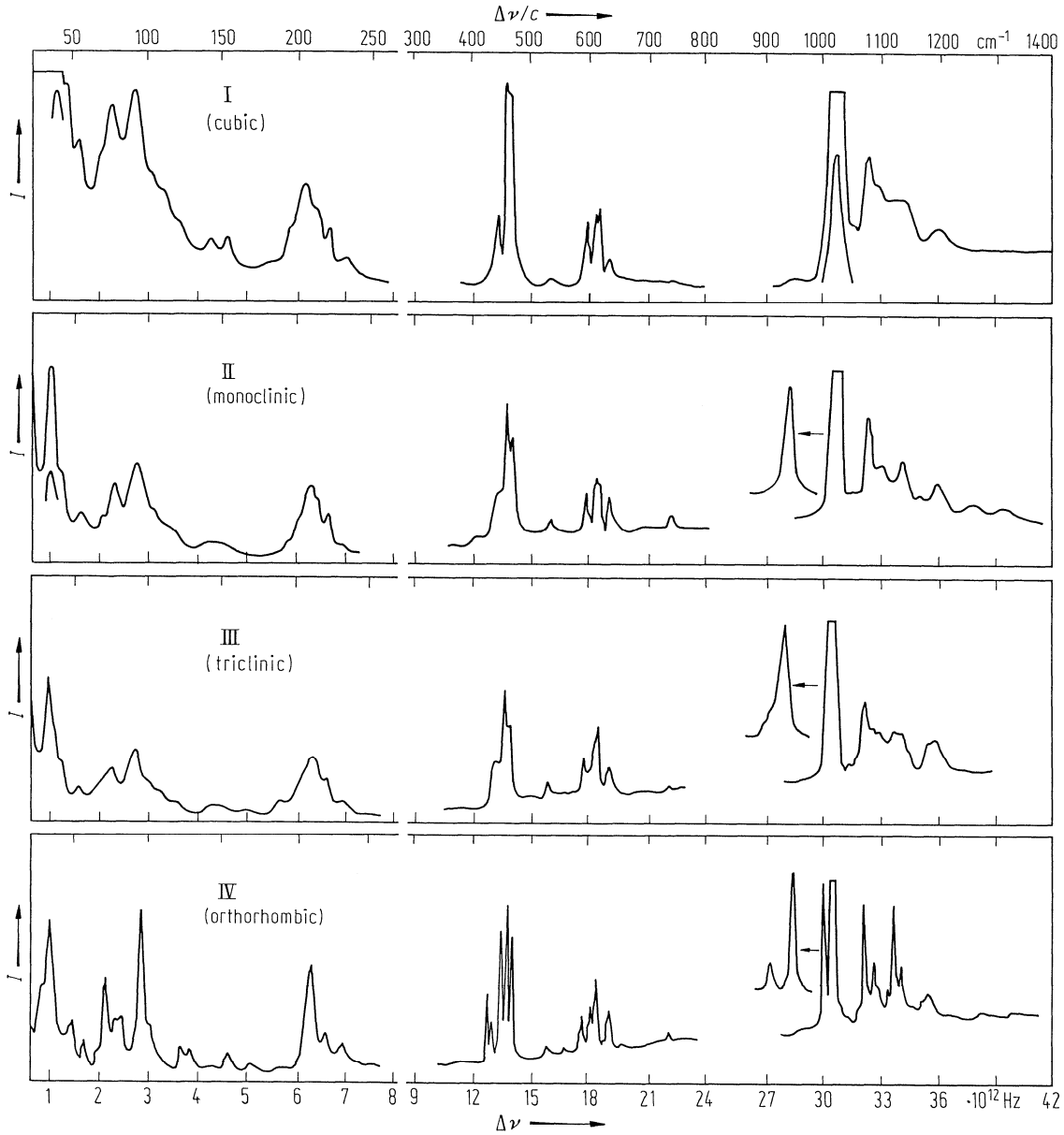

Fig. 43A-15-011. $Tl_2Cd_2(SO_4)_3$. Depolarized Raman spectra in four phases [82Kre].

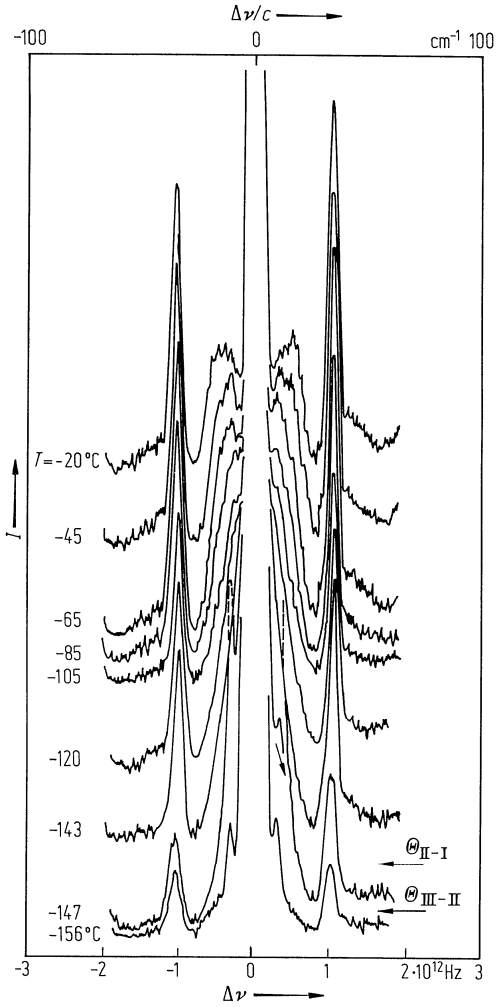

Fig. 43A-15-012. $Tl_2Cd_2(SO_4)_3$. I vs. $\Delta\nu$ [79Rab]. I: Raman scattering intensity. Scattering geometry: *Z(XX)Y*. Parameter: T.

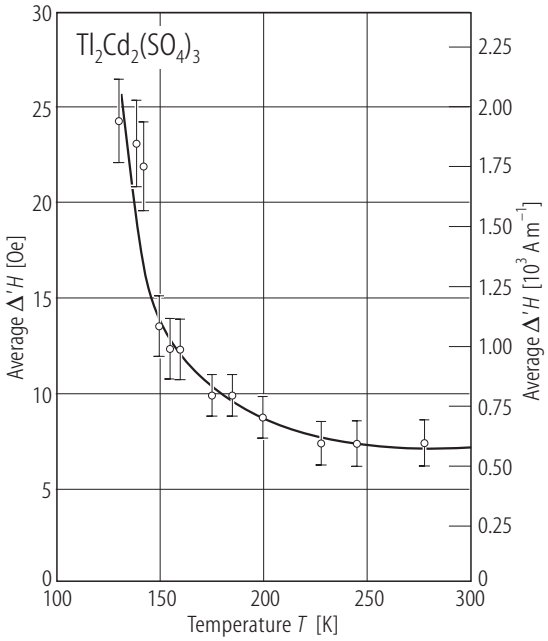

Fig. 43A-15-013. $Tl_2Cd_2(SO_4)_3$:Mn^{2+}. Δ'*H* vs. *T* [87Mis]. Δ'*H*: average of the three highest-field lines for Mn^{2+} ESR. $H \parallel \langle 100 \rangle$.